PLOS ONE

RESEARCH ARTICLE

Low Dose PET Image Reconstruction with Total Variation Using Alternating Direction Method

Xingjian Yu[1], Chenye Wang[1], Hongjie Hu[2], Huafeng Liu[1]*

1 State Key Laboratory of Modern Optical Instrumentation, Department of Optical Engineering, Zhejiang University, Hangzhou, China, **2** Sir Run Run Shaw Hospital, Zhejiang University, Hangzhou, China

* liuhf@zju.edu.cn

Citation: Yu X, Wang C, Hu H, Liu H (2016) Low Dose PET Image Reconstruction with Total Variation Using Alternating Direction Method. PLoS ONE 11(12): e0166871. doi:10.1371/journal.pone.0166871

Editor: Li Zeng, Chongqing University, CHINA

Received: April 21, 2016

Accepted: November 4, 2016

Published: December 22, 2016

Data Availability Statement: The original data includes Monte Carlo simulated brain phantom, Deremzo phantom and Zubal thorax phantom and the data from the clinical patient. Among them, The brain phantom comes from the Hoffman brain phantom. The Derenzo phantom is the widely used phantom for sptial resolution in PET community. The phantom data is an open source kind of data. The Derenzo data could be accessed at https://figshare.com/articles/Derenzo_phantom_and_data/3492260. The zubal phantom could be accessed at: http://noodle.med.yale.edu/zubal/data.htm, and the brain phantom could be accessed at http://www.fil.ion.ucl.ac.uk/spm/data/motor/. The data from

Abstract

In this paper, a total variation (TV) minimization strategy is proposed to overcome the problem of sparse spatial resolution and large amounts of noise in low dose positron emission tomography (PET) imaging reconstruction. Two types of objective function were established based on two statistical models of measured PET data, least-square (LS) TV for the Gaussian distribution and Poisson-TV for the Poisson distribution. To efficiently obtain high quality reconstructed images, the alternating direction method (ADM) is used to solve these objective functions. As compared with the iterative shrinkage/thresholding (IST) based algorithms, the proposed ADM can make full use of the TV constraint and its convergence rate is faster. The performance of the proposed approach is validated through comparisons with the expectation-maximization (EM) method using synthetic and experimental biological data. In the comparisons, the results of both LS-TV and Poisson-TV are taken into consideration to find which models are more suitable for PET imaging, in particular low-dose PET. To evaluate the results quantitatively, we computed bias, variance, and the contrast recovery coefficient (CRC) and drew profiles of the reconstructed images produced by the different methods. The results show that both Poisson-TV and LS-TV can provide a high visual quality at a low dose level. The bias and variance of the proposed LS-TV and Poisson-TV methods are 20% to 74% less at all counting levels than those of the EM method. Poisson-TV gives the best performance in terms of high-accuracy reconstruction with the lowest bias and variance as compared to the ground truth (14.3% less bias and 21.9% less variance). In contrast, LS-TV gives the best performance in terms of the high contrast of the reconstruction with the highest CRC.

Introduction

Positron emission tomography (PET) is a nuclear image modality that can produce 3D functional images of biological processes inside the human body [1]. PET has now become an indispensable tool in cardiac/brain research and cancer diagnosis/treatment. However, the reconstruction of low-dose PET images has remained a challenge because of the large amount

patient can be accessed at http://web.eecs.umich.edu/~fessler/result/et/pet,emis/.

Funding: This work is supported in part by the National Natural Science Foundation of China (No: 61427807, 61271083, 61525106), by National Key Technology Research and Development Program of the Ministry of Science and Technology of China (No: 2016YFC1300302), by the Shenzhen Innovation Funding (SGLH20131010110119871), by Zhejiang Province Science and Technology Projects (No: 2015C33061). The funders had no role in study design, data collection and analysis, decision to publish, or preparation of the manuscript.

Competing Interests: The authors have declared that no competing interests exist.

Abbreviations: TV, Total variation; ADM, Alternating direction method; EM, Expectation-maximization; Poisson-TV, Poisson total variation; LS-TV, Least square total variation; MAP, Maximum a posteriori; PWLS, Penalized weighted lease-squares; SNR, Signal-to-noise ratio; SOCP, Second-Order cone program; LOR, Line of response; BB, Barzilai and Borwein; CRC, Contrast recovery coefficient; ROI, Region of interest; FOV, Field of view.

of noise and the sparse spatial resolution [2]. To meet the challenge, researchers have proposed a number of different iterative statistical methods to reconstruct the PET images based on different statistical assumptions of PET measurements, such as maximum likelihood (ML), expectation maximization (EM) [3–5], maximum a posteriori (MAP) [6–8], and penalized weighted least-squares (PWLS) [9, 10]. Nevertheless, these iterative statistical methods still have several drawbacks. For example they cannot easily handle low signal-to-noise ratio (SNR) data. Furthermore, after the subtraction of random events, the corrections for scanner sensitivity and dead time, and the corrections for attenuation and scatter, the actual statistical property of measured data is quite complex and it does not exactly follow the Poisson distribution [11, 12].

The nature of PET images is an additional factor to consider in PET image reconstruction [13]. One important PET image feature is the edge. The edge information usually represents the sharp variation in images, such as the object boundaries, which is very important and useful for clinical diagnosis, e.g., of tumors [14]. Given the nature of PET images, researchers have proposed total variation (TV) based methods for both the image space and the projection space in PET image reconstruction [15]. TV was incorporated to provide edge-preserving guidance for the reconstruction [15], and it is well known that it suppresses noise effectively while preserving sharp edges [16–18]. Based on the complexity of the statistical property of PET data, there should be several types of TV-constraint PET imaging models for different statistical assumptions. However, there have been no discussions or research studies on this point in the PET imaging community. In contrast, two types of TV incorporated models have been developed in the image processing community: Gaussian-TV [19] and Poisson-TV [20]. The Gaussian-TV model includes an energy functional to control the type of smoothness of solutions. The Poisson-TV model includes a Poisson data fidelity term to meet the statistical assumption. Both can be used for PET image reconstruction theoretically. However, it remains unknown which one is the better choice for various PET application areas. For example, the low bias and variance of the reconstructed image is more important for kinetic estimation, whereas high contrast is required for tumor diagnosis. In addition, a complication of the TV model is the strong nonlinearity in the data fidelity, and therefore, problems or issues arise in the computation of minimizers [20].

There are three classes of existing solvers for the TV problem. Algorithms in the first class are based on smoothing the TV term, since TV is non-smooth, which causes the main difficulty in solving the TV problem. A number of methods based on smoothing have been proposed, one of which is the second-order cone program (SOCP) [21, 22]. The SOCP solver reformulates TV minimization as a second order cone programming problem [22], which can be solved by interior-point algorithms. The SOCP solver can easily be adapted to various convex TV models with distinct terms and constraints with high accuracy. However, the speed of SOCP is very slow, because it embeds the interior-point algorithm and directly solves a linear system at each iteration. The second class of algorithms for TV problems comprises those based on the iterative shrinkage/thresholding (IST) algorithms, which have been proposed by several researchers in the last few years [23–26]. IST is able to minimize the TV constraint term with some non-quadratic and non-smooth regularization terms. The convergence rate of IST algorithms heavily relies on the linear observation operator, and the convergence rate of algorithms in this class is not sufficiently fast. Furthermore, IST-based algorithms for TV deconvolution require that a de-noising subproblem be solved at each iteration and they cannot take advantage of problem structures. The third class of algorithms for TV problems comprises those based on seeking the minimizer or maximizer of the original constrained problem by a sequence of unconstrained subproblems. Methods belonging to this class add a quadratic penalty term instead of the normal constraint term in the objective function. The penalty term is

the square of the constraint violation with the multiplier. Because of its simplicity and intuitive appeal, this approach is widely used. The well-known augmented Lagrangian method (ALM) [27, 28] belongs to this class. In the augmented Lagrangian method, the Lagrangian multiplier is introduced and is estimated at each iteration in the objective function. However, it requires that multipliers go to infinity to guarantee the convergence, which may cause the ill-condition problem numerically.

To overcome the issue that the solvers mentioned above are weak in terms of efficiency and robustness, in this study an alternating direction method (ADM) was applied [29, 30] to solve the TV problem. The proposed ADM constitutes implementable variants of the classical ALM for optimization problems with separable structures and linear constraints. In this method, the TV regularization term is split into two terms with the aid of a new slack variable so that an alternating minimization scheme can be coupled to minimize the approximate objective function. This split and the use of the alternating minimization scheme not only accelerate the convergence rate of the solution, but also result in improved accuracy, as well as in robustness of the reconstructed results to the noise in the data set.

We used Monte Carlo simulated data, phantom data, and real patient data to validate the performance of the proposed algorithm as perceived both quantitatively and visually. Experimental results show that the proposed algorithm is highly effective in preserving sharp image edges and more details while eliminating staircase artifacts. In addition, the performances of the Poisson-TV and LS-TV methods on PET data at different counting levels are also evaluated in this work.

The rest of this paper is organized as follows. In Section 2, first the PET imaging model is reviewed, and then, two objective functions and the corresponding method to solve them are suggested. In Section 3, the experimental setup, results, and comparisons of the existing methods and the proposed methods are presented. Section 4 constitutes the conclusion.

Materials and Methods

PET imaging model

PET acquired data are organized in a series of parallel slices that can be reconstructed independently. Every slice of raw data collected by a PET scanner constitutes a list of coincidence events representing near-simultaneous detection of annihilation photons by a pair of detectors. Each coincidence event represents a line in space connecting the two detectors along which the positron emission occurred (the line of response (LOR)). The raw data from PET are organized in a sinogram.

Therefore, PET image reconstruction problems are specific cases of the following general inverse problem: find an estimate of radioactive activity map u from a measurement b by

$$b = Au + noise \tag{1}$$

In the process of PET imaging reconstruction, u is the reconstruction image and A is the system matrix that describes the tomographic geometry and the physical factors.

LS-TV

Problem formulation. Assuming piecewise constant behavior of PET images, we introduce total variation (TV) regularization into PET reconstruction.

The problem is formulated as

$$\min_u TV(u), s.t.\ \ Au = b \tag{2}$$

where $TV(u)$ is the PET reconstruction with the TV defined regularization; it is defined as $\Sigma_i\|D_iu\|$, the sum of the discrete gradient of activity map u of every pixel i.

Solution. It is difficult to directly obtain the solution of Eq (2). Therefore, we introduce a new auxiliary variable, w. At each pixel, an auxiliary variable w_i is introduced into the term $\|.\|$. The purpose of this process is to transfer D_iu out of $\|.\|$. The optimization problem of Eq (2) is clearly equivalent to

$$\min_{w_i,u} \sum_i \| w_i \|, \quad s.t. \quad Au = b \text{ and } D_iu = w_i \text{ for all } i \tag{3}$$

To deal with the constraints, we transform the constrained Problem (3) to an equivalent unconstrained problem using an augmented Lagrangian function [31]. The corresponding augmented Lagrangian function of Problem (3) is

$$\begin{aligned} L_A(w_i,u) &= \sum_i (\| w_i \| - \upsilon_i^T(D_iu - w_i) \\ &\quad + \frac{\beta_i}{2} \| D_iu - w_i \|_2^2) - \lambda^T(Au - b) + \frac{\mu}{2} \| Au - b \|_2^2 \end{aligned} \tag{4}$$

where υ_i, β_i, λ, and μ are the multipliers of the four penalty terms. The first term of Eq (4) is the regularization term, and the remaining terms are penalty terms. The second and fourth terms are linear parts, whereas the third term and fifth terms are quadratic parts. These parts ensure the accuracy and robustness of the TV constraint. In order to make the result of every term a number rather than a matrix, transposition of υ and λ is utilized in Eq (4). To solve Eq (4) efficiently, the ADM, which was originally proposed to handle parabolic and elliptic differential equations, was embedded here. This algorithm is a variant of the classical ALM. When the classical ALM approaches the solutions of the original Problem (4), the nice separable structure emerging from Eq (4) in both the objective function and the constraint is weaker. This drawback, however, can be completely overcome by the ADM. In the ADM, the solution of Eq (4) is transformed to solve three subproblems at each iteration for variables u_k and $w_{i,k}$ and parameters λ and υ.

In ADM, let u_k and $w_{i,k}$ represent the true minimizers of Eq (4) at the kth iteration. $w_{i,k+1}$ can be attained by

$$\begin{aligned} \min_{w_i} L_A(w_i,u_k) &= \sum_i (\| w_i \| - \upsilon_i^T(D_iu_k - w_i) \\ &\quad + \frac{\beta_i}{2} \| D_iu_k - w_i \|_2^2) - \lambda^T(Au_k - b) + \frac{\mu}{2} \| Au_k - b \|_2^2 \end{aligned} \tag{5}$$

To solve this minimization problem, Eq (5) can be separated as two subproblems for variables u and w based on ADM. We first fix the value of u and calculate the solution of w. Therefore, only the terms containing w are useful. The corresponding subproblem can be expressed as the following problem:

$$w_i = \arg\min_{w_i} L_A(w_i,u_k) = \min_{w_i} \sum_i \left(\| w_i \| - \upsilon_i^T(D_iu - w_i) + \frac{\beta_i}{2} \| D_iu - w_i \|_2^2 \right) \tag{6}$$

For given $\beta > 0$, the minimizer of Eq (6) is given by the 2D shrinkage-like formula [32]. $w_{i,k+1}$ can be calculated by

$$w_{i,k+1} = \max \left\{ \| D_iu_k - \frac{\upsilon_i}{\beta_i} \| - \frac{1}{\beta_i}, 0 \right\} \frac{\left(D_iu_k - \frac{\upsilon_i}{\beta_i} \right)}{\| D_iu_k - \frac{\upsilon_i}{\beta_i} \|} \tag{7}$$

With $w_{i,k+1}$, we can achieve u_{k+1} by

$$\begin{aligned}\min_u L_A(w_{i,k+1},u) &= \sum_i (\| w_{i,k+1} \| - v_i^T(D_i u_k - w_{i,k+1}) \\ &+ \frac{\beta_i}{2}\| D_i u_k - w_{i,k+1} \|_2^2) - \lambda^T(Au_k - b) + \frac{\mu}{2}\| Au_k - b \|_2^2\end{aligned} \tag{8}$$

The constant terms do not influence the minimum, and thus, this subproblem is equivalent to the problem

$$\begin{aligned}u &= \arg\min_u L_A(w_{i,k+1},u) = \min_u \sum_i (-v_i^T(D_i u_k - w_{i,k+1}) \\ &+ \frac{\beta_i}{2}\| D_i u_k - w_{i,k+1} \|_2^2) - \lambda^T(Au_k - b) + \frac{\mu}{2}\| Au_k - b \|_2^2\end{aligned} \tag{9}$$

Its gradient is

$$d_k(u) = \sum_i (\beta_i D_i^T(-D_i u - w_{i,k+1}) + \mu A^T(Au - b) - A^T\lambda - D_i^T v_i) \tag{10}$$

By enforcing $d_k(u) = 0$, we can obtain the exact minimizer of Eq (9) directly. However, this calculation is too costly to implement numerically, in particular when the matrix is large. To obtain u_{k+1} more efficiently, the steepest descent method with an appropriate step length is used iteratively by applying the recurrence formulation:

$$u_{k+1} = u_k - \alpha_k d_k(u_k) \tag{11}$$

where α_k is the step length. Each iteration of the steepest descent method demands that the gradient be updated to update the estimation value of u_{k+1}. Therefore, the step length should be chosen carefully to obtain an accurate solution.

It remains to choose α. It is suggested that the aggressive manner [33–35] be used to choose the step length for the steepest descent method, which is called the BB (Barzilai and Borwein) step or BB method. This method is applied to choose α:

$$\alpha_k = \frac{(u_k - u_{k-1})^T(u_k - u_{k-1})}{(u_k - u_{k-1})^T(d_k(u_k) - d_k(u_{k-1}))} \tag{12}$$

Parameters. There are several parameters in the algorithm. Among these, β, v_i, and λ are initialized as 1, 1, **1**, based on [36]. μ is the most important parameter, since it determines the weight of the data fitting term. Therefore, to achieve the best performance, the value of μ should be set according to the noise level in observation b. For example, the higher the noise level is, the smaller μ should be. μ was manually tuned in this study. v_i and λ should be updated provided that Eq (4) is minimized at each iteration. According to the formula proposed by Hestenes and Powell [28, 37–40], the update formulas of multipliers follow

$$v_{i,k+1} = v_{i,k} - \beta_{i,k}(D_i u_k - w_{i,k}) \tag{13}$$

$$\lambda_{k+1} = \lambda_k - \mu_k(Au_k - b) \tag{14}$$

The program terminates after a certain number of iterations (300 in this study), or when the relative stopping criterion (based on empirical estimations) is reached:

$$\epsilon = \frac{\| u^{k+1} - u^k \|}{\| u^k \|} < 10^{-3} \tag{15}$$

Poisson-TV

Problem formulation. Because of the issue of the low SNR and the Poisson distribution of PET measurements, we build the objective function as

$$\min_u TV(u) + \mu \sum_i (\bar{b}_i - b_i \log \bar{b}_i), s.t.\ Au = b \tag{16}$$

Solution. To solve the objective function in Eq (16), the ADM is also used to solve some subproblems at each iteration to approach a solution of Eq (16). We add two auxiliary variables, Z_S and S, into the function, as in Eq (3). Then, we construct the augmented Lagrangian objective function for Eq (16):

$$\min_u\ TV(u) + \mu \sum_i (\bar{b}_i - b_i \log \bar{b}_i) - < Z_S, S - u > + \frac{\beta_S}{2} \| S - u \|_F^2 \tag{17}$$

In a more compact form, we have

$$\min_u \sum_i \| Du_i \| + \mu \sum_i (\bar{b}_i - b_i \log \bar{b}_i) + \frac{\beta_S}{2} \| S - u - \frac{Z_S}{\beta_S} \|_F^2 \tag{18}$$

We can obtain u by

$$\min_u \sum_i \| Du_i \| + \frac{\beta_S}{2} \| S - u - \frac{Z_S}{\beta_S} \|_F^2 \tag{19}$$

where the u sub-problem is solved by an EM-like method. We rewrite the objective function with items containing only u and take the expectation step with respect to the unobservable variables $w_i j$ and calculate the surrogate function.

$$F(u) = \mu \sum_{m=1}^{n_m} \left(\sum_{j=1}^{n_j} \left[\sum_{i=1}^{n_i} (u_{jm} aij - w_{ij}^m log(g_{ij} S_{jm})) \right] \right) \tag{20}$$

We minimize this surrogate function F by zeroing its derivative with respect to S_{jm}:

$$\frac{\partial F}{\partial S_{jm}} = \mu \sum_{m=1}^{n_i} g_{ij} - \frac{\mu}{S_{jm}} \sum_{i=1}^{n_i} w_{ij}^m = 0 \tag{21}$$

Thus, x_{jm}^{k+1} is the root of

$$S_{jm}^2 + \left(\mu \sum_{i=1}^{n_i} g_{ij} \right) x_{jm} - \mu \sum_{i=1}^{n_i} w_{ij}^m = 0 \tag{22}$$

Finally, the updating rule for x_{jm}^{k+1} is

$$x_{jm}^{k+1} = \frac{-(\mu \sum_{i=1}^{n_i} g_{ij}) + \sqrt{(\mu \sum_{i=1}^{n_i} g_{ij})^2 + 4\mu \sum_{i=1}^{n_i} w_{ij}^m}}{2} \tag{23}$$

Moreover, Z_S in Eq (19) is updated as

$$Z_S^{k+1} = Z_S^k - \beta_S(u^{k+1} - S^{k+1}) \tag{24}$$

Convergence analysis

The analysis of the convergence properties of the proposed TV regulation process is presented in this section. β and β_S strongly affect convergence in both the Poisson-TV and LS-TV methods. The selection of these parameters also affects the convergence rate of the proposed method. The convergence of the sequence (w and u) in the Poisson-TV and (u and S) in the LS-TV was proven in the convergence analysis section in [32, 41]. It has been proven that the proposed method can converge to the final solutions from any initial points. To demonstrate the effectiveness of the ADM, we also provide a comparison of the convergence speed of the proposed method and IST method (a detailed description of this is algorithm is given in [23]) in the results section.

Ethics Statement

Before the Results section, we state that no human and animal research was involved in this work.

Results

In this section, to validate and evaluate the proposed method, the results of simulation and clinical experiments are presented. In the Monte Carlo simulation experiments, a Hoffman brain phantom and Zubal phantom were used and we simulated projections using GATE [42]. All the tests were performed using MATLAB on a PC with an Intel i7-3770 3.40 GHz and 8 GB RAM. In the clinical experiment, we applied our method to a typical PET scanner. All the scans were executed using a Hamamatsu PET scanner. To obtain a good visual effect of our method, we compared the EM [43], Poisson-TV, and LS-TV methods.

Monte Carlo simulations

The scanner simulated in GATE was the Hamamatsu SHR-22000 scanner, which consists of 32 rings with 24576 (3072/ring) BGO crystals of $2.8mm * 6.95mm * 30mm$, 768 PMTs, and an 838 mm detector ring diameter. The activity maps of the Hoffman brain phantom (Fig 1(a)) and Zubal phantom (Fig 1(b)) were used as the ground truths. The sinograms calculated from the ground truths by GATE were used as the measurements for our tests. All the tests were performed using MATLAB on a PC with an Intel i7-3770 3.40 GHz and 8 GB RAM. The system matrix G used for matching the dimensions of the simulated sinogram was generated by the Fessler tomography toolbox [44].

Both the EM and our model-based TV method were applied to reconstruct the activity maps from the Monte Carlo simulation measurements. The ability of two frameworks (the EM and model-based TV method) to reconstruct a PET activity map was compared in this experiment. This ability is quantified using the relative errors bias, variance, and contrast recovery

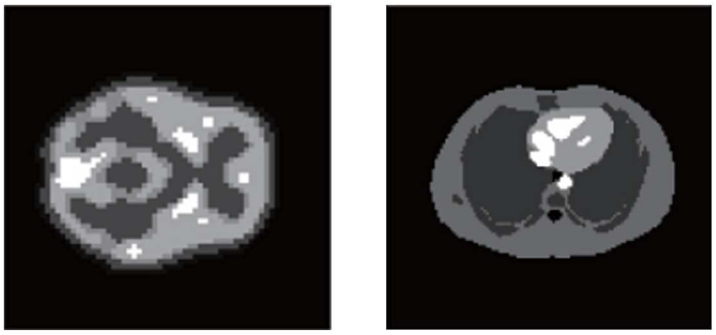

(a) Hoffman brain phantom (b) Zubal phantom

Fig 1. Ground truths of the Monte Carlo simulation.

doi:10.1371/journal.pone.0166871.g001

coefficient (CRC) of the region of interest (ROI) calculated as

$$bias = \frac{1}{n}\sum_{i=1}^{n}(\hat{u}_i - u_i) \tag{25}$$

$$variance = \frac{1}{n}\sum_{i=1}^{n}(\hat{u}_i - u_i)^2 \tag{26}$$

$$CRC = \frac{Contrast_{measure}}{Contrast_{theory}} = \frac{(S/B)_{measure} - 1}{(S/B)_{theory} - 1} \tag{27}$$

where u_i is the ith pixel of ground truth u and $\hat{u}_i$ is the ith pixel of the reconstructed images. S is the mean activity of the ROI and B is the mean activity of the white matter region (background) in the reconstructed image. The bias and variance are used to evaluate the accuracy of the reconstruction and CRC is used to indicate the relative contrast of the ROI in the reconstructed images.

In our method, the TV factor (the value of weighting parameter μ) is an important parameter, which can be optimized to smoothen the results. To study the impact of the initial condition of the TV factor in our method, we plotted the bias curve and variance curve versus the TV factor, which are shown in Fig 2. When the TV factor increases, the bias and variance curves first decrease and then increase. Therefore, we can choose the nadir value of the curve as the optimized TV factor, which is 0.0025 in Poisson-TV and 4 in LS-TV for all experiments at all count levels.

The activity maps of Hoffman brain phantom and Zubal phantom reconstructed by the EM and the proposed TV methods are presented in Figs 3 and 4. The sinograms used in Figs 3 and 4 constitute high count level data; the count is approximately 10^7. This clearly indicates that the quality of recovery of both Poisson-TV and LS-TV is much higher than that of the EM method. In addition, the reconstructed images also indicate that the edge of the reconstruction produced by the proposed methods is sharper. However, the LS-TV method yields sharper edge information than does Poisson-TV. To evaluate the accuracy of the reconstruction, we marked the specific region of the images (Figs 3(b) and 4(b)) for quantitative analysis. In addition, we present the profiles of the reconstructed images by all methods in the Fig 5. It is clear that the results of Poisson-TV give the closest fit to the ground truth.

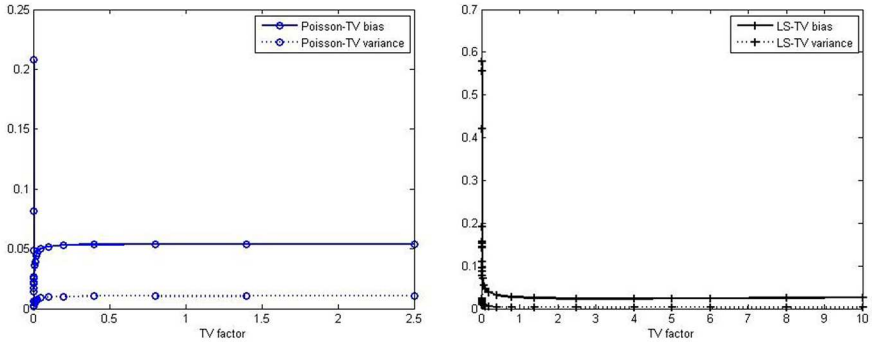

(a) Bias and variance versus TV factor for LS-TV bias (b) Variance versus TV factor for Poisson-TV

Fig 2. Profile of the bias and variance versus TV factor.

doi:10.1371/journal.pone.0166871.g002

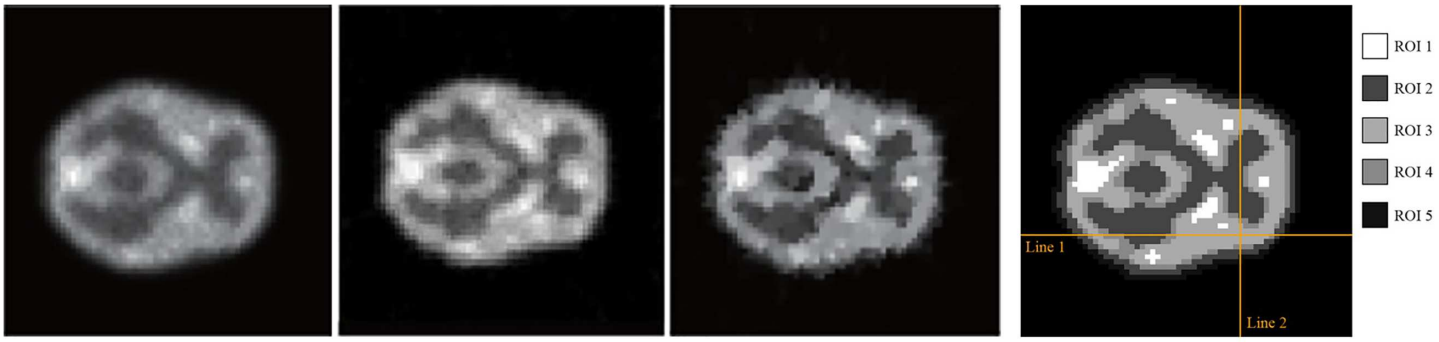

(a) Images (brain phantom) reconstructed by EM, Poisson-TV, and LS-TV (from left to right) (b) Marked regions of the images

Fig 3. Reconstruction of the brain phantom.

doi:10.1371/journal.pone.0166871.g003

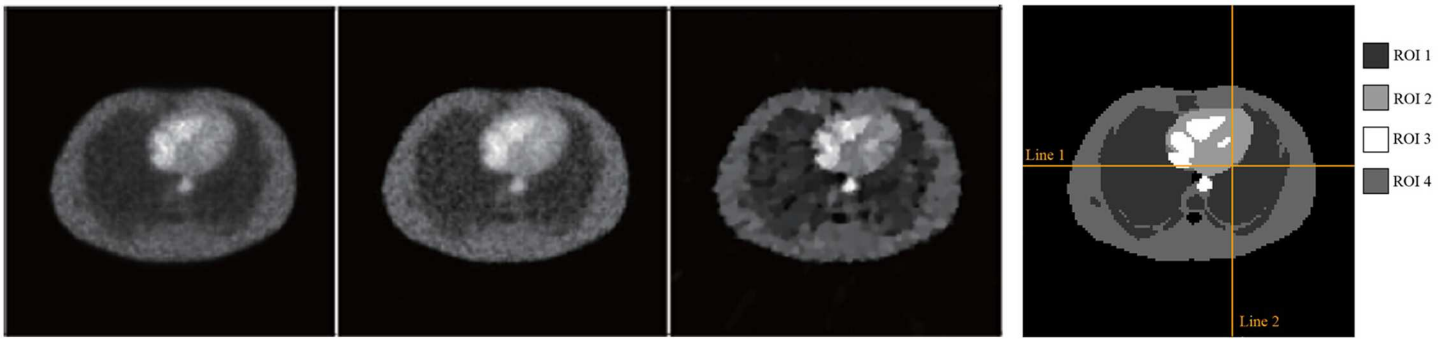

(a) Images (Zubal phantom) reconstructed by EM, Poisson-TV, and LS-TV (from left to right) (b) Marked regions of the images

Fig 4. Reconstruction of the Zubal phantom.

doi:10.1371/journal.pone.0166871.g004

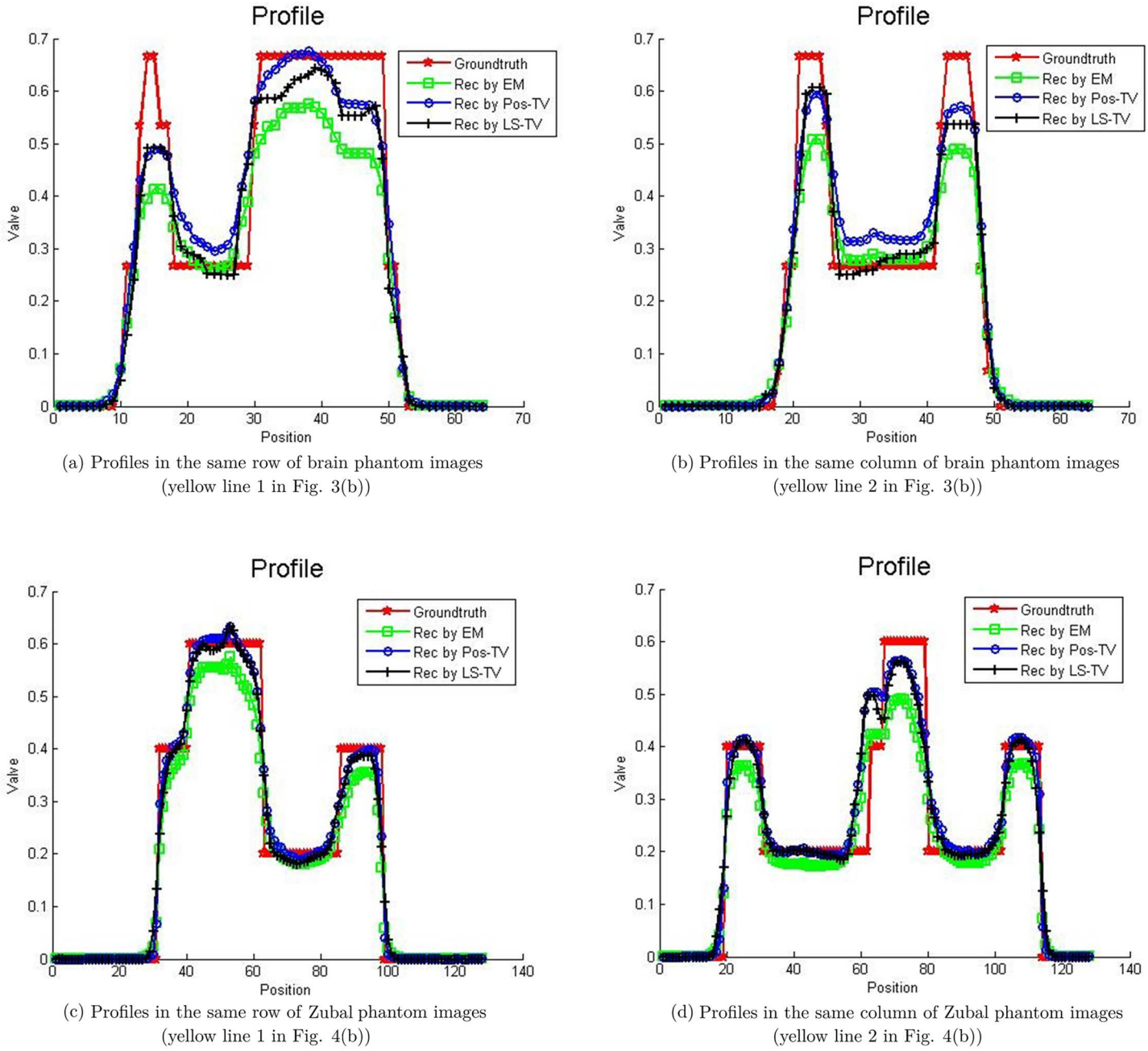

(a) Profiles in the same row of brain phantom images (yellow line 1 in Fig. 3(b))

(b) Profiles in the same column of brain phantom images (yellow line 2 in Fig. 3(b))

(c) Profiles in the same row of Zubal phantom images (yellow line 1 in Fig. 4(b))

(d) Profiles in the same column of Zubal phantom images (yellow line 2 in Fig. 4(b))

Fig 5. Profiles of the marked region of the brain phantom.

doi:10.1371/journal.pone.0166871.g005

To evaluate the performance of the Poisson-TV and LS-TV methods at different count (dose) levels, five counting level values (total number of photon counts in the reconstruction plane: $5 * 10^5$, $1 * 10^6$, $3 * 10^6$, $6 * 10^6$ and $9 * 10^6$) were simulated in this experiment.

The activity maps of the Hoffman brain phantom (Fig 6(a)) and Zubal phantom (Fig 6(b)) reconstructed by EM, Poisson-TV, and LS-TV from the data with different numbers of counts are given in Fig 6. Tables 1 and 2 list the bias and variance of EM, Poisson-TV, and LS-TV for the different counting level data. This demonstrates the statistical analysis of the reconstructed

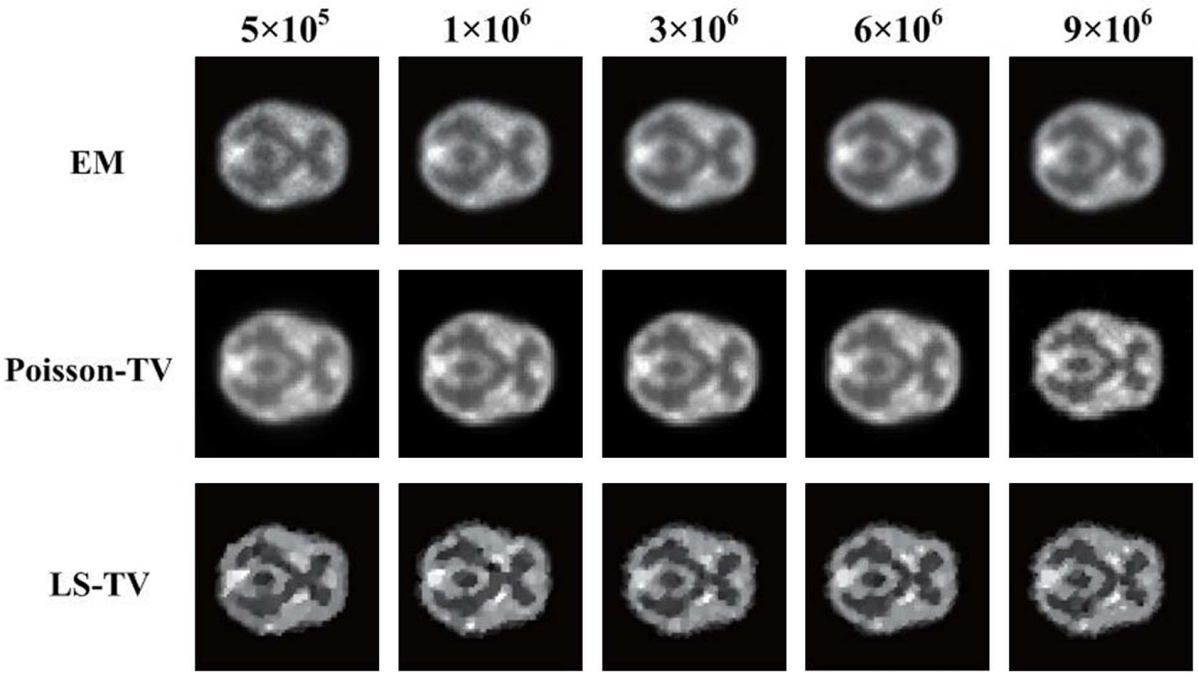

(a) Brain images reconstructed by EM (first row), images reconstructed by Poisson-TV (second row), and images reconstructed by LS-TV (third row) from the data with a different number of counts. From left to right: $5*10^5, 1*10^6, 3*10^6, 6*10^6$, and $9*10^6$

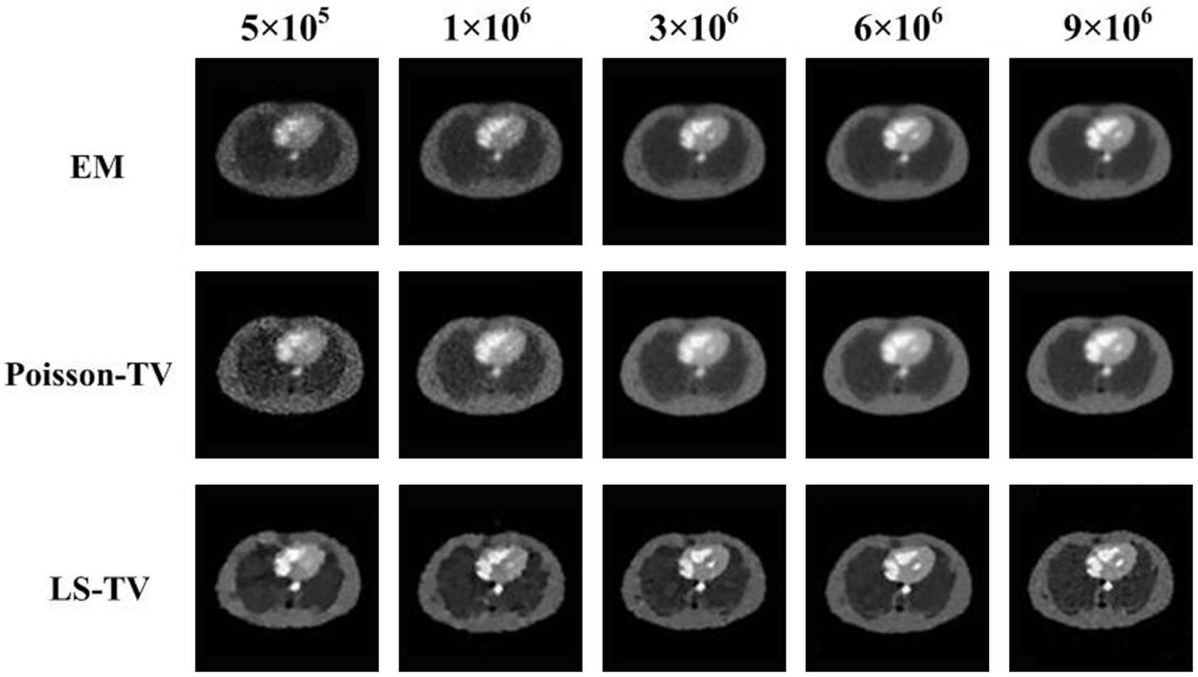

(b) Zubal images reconstructed by EM (first row), images reconstructed by Poisson-TV (second row), and images reconstructed by LS-TV (third row) from the data with a different number of counts. From left to right: $5*10^5, 1*10^6, 3*10^6, 6*10^6$, and $9*10^6$.

Fig 6. Reconstruction of the EM, LS-TV, and Poisson-TV for the data with different counts.

doi:10.1371/journal.pone.0166871.g006

Table 1. Quantitative analysis of the reconstructions by EM, Poisson-TV, and LS-TV for Zubal phantom.

	Counting	Zubal Phantom					
		Bias			Variance		
		EM	LSTV	PosTV	EM	LSTV	PosTV
Total	5E5	0.0327	0.0312	**0.0286**	0.0043	0.0039	**0.0033**
	1E6	0.0262	0.0214	**0.0206**	0.0029	0.0021	**0.0020**
	3E6	0.0218	0.0205	**0.0195**	0.0022	**0.0018**	0.0019
	6E6	0.0198	0.0196	**0.0185**	0.0020	0.0017	**0.0017**
	9E6	0.0186	0.0181	**0.0166**	0.0018	**0.0014**	0.0015
ROI 1	5E5	0.3995	**0.2653**	0.3527	0.2114	**0.0864**	0.1725
	1E6	0.3275	**0.2031**	0.3101	0.1541	**0.0657**	0.1455
	3E6	0.2613	**0.1604**	0.1925	0.0789	**0.0425**	0.0571
	6E6	0.2460	**0.1825**	0.1874	0.0626	**0.0492**	0.0523
	9E6	0.1876	**0.1093**	0.1431	0.0236	**0.0186**	0.0309
ROI 2	5E5	0.1715	**0.1005**	0.1459	0.0436	**0.0193**	0.0275
	1E6	0.1415	**0.0777**	0.1088	0.0385	**0.0122**	0.0227
	3E6	0.1307	**0.0586**	0.0943	0.0303	**0.0064**	0.0164
	6E6	0.0735	**0.0524**	0.0642	0.0098	**0.0051**	0.0075
	9E6	0.0521	**0.0348**	0.0412	0.0054	**0.0025**	0.0038
ROI 3	5E5	0.1766	**0.0946**	0.1063	0.0672	**0.0163**	0.0186
	1E6	0.1478	**0.0742**	0.0848	0.0427	**0.0130**	0.0147
	3E6	0.1120	**0.0588**	0.0637	0.0222	0.0077	**0.0073**
	6E6	0.0896	**0.0419**	0.0499	0.0149	0.0054	**0.0051**
	9E6	0.0686	**0.0404**	0.0446	0.0101	0.0052	**0.0048**
ROI 4	5E5	0.1954	**0.1122**	0.1965	0.0865	**0.0186**	0.0822
	1E6	0.1679	**0.0960**	0.1591	0.0595	**0.0186**	0.0539
	3E6	0.1510	**0.0829**	0.1378	0.0432	**0.0155**	0.0366
	6E6	0.1407	**0.0751**	0.1207	0.0387	**0.0131**	0.0281
	9E6	0.0869	**0.0533**	0.0756	0.0174	**0.0070**	0.0132

doi:10.1371/journal.pone.0166871.t001

results, which confirms that our model yields better estimates in terms of bias when the counting level changes. The robustness of the proposed method to noise was also evaluated by sinogram data with different counting levels (a lower count means more serious noise). As indicated in Tables 1 and 2, the variance of the Poisson-TV and LS-TV methods is 22% to 74% less than that of the EM method at all counting levels. In other words, the proposed method is more robust to noise than EM. Moreover, Table 1 also shows that the bias and variance for LS-TV and Poisson-TV decrease faster than those of EM when the counting level increases. For a full comparison, the bias, variance, and CRC curves of EM, Poisson-TV, and LS-TV in ROI 1, 2, and 3 for the brain and Zubal phantoms are given in Fig 7. Fig 7(a) and 7(b) show the bias curves. The bias curve for the EM was not improved significantly when the counting level increased, whereas the bias curve for our method decreased. Fig 7(c) and 7(d) show the variance curves, which exhibit the same trend as Fig 7(a) and 7(b). Fig 7(e) and 7(f) show the CRC curves. All the CRC curves increase when the counting level increases, whereas the CRC curves for the proposed method increase faster and higher, and LS-TV gives the best CRC in all methods.

Furthermore, we plotted the relative error of reconstruction after each iteration of the algorithms to evaluate the convergence speed of the Poisson-TV, LS-TV, EM, and IST methods.

Table 2. Quantitative analysis of the reconstructions by EM, Poisson-TV, and LS-TV for brain phantom.

	Counting	Zubal Phantom					
		Bias			Variance		
		EM	LSTV	PosTV	EM	LSTV	PosTV
Total	5E5	0.0357	0.0319	**0.0273**	0.0134	0.0119	**0.0098**
	1E6	0.0334	0.0281	**0.0249**	0.0123	0.0102	**0.0086**
	3E6	0.0329	0.0275	**0.0223**	0.0116	0.0089	**0.0075**
	6E6	0.0329	0.0263	**0.0201**	0.0116	0.0078	**0.0069**
	9E6	0.033	0.0248	**0.0195**	0.0116	0.0069	**0.0064**
ROI 1	5E5	0.1321	0.0776	**0.0400**	0.0372	0.0132	**0.0037**
	1E6	0.0834	0.0444	**0.0298**	0.0143	0.0054	**0.0022**
	3E6	0.0620	0.0464	**0.0294**	0.0083	0.0054	**0.0021**
	6E6	0.0423	0.0391	**0.0203**	0.0046	0.0045	**0.0012**
	9E6	0.0337	0.0301	**0.0136**	0.0032	0.0025	**0.0006**
ROI 2	5E5	0.2198	0.2068	**0.0945**	0.0882	0.0779	**0.0168**
	1E6	0.1723	0.1568	**0.0708**	0.0547	0.0488	**0.0090**
	3E6	0.1297	0.1272	**0.0649**	0.0331	0.0292	**0.0079**
	6E6	0.1235	0.1102	**0.0563**	0.0318	0.0222	**0.0060**
	9E6	0.1189	0.0624	**0.0482**	0.0292	0.0091	**0.0054**
ROI 3	5E5	0.1570	0.1051	**0.0780**	0.0479	0.0223	**0.0120**
	1E6	0.1183	0.0591	**0.0448**	0.0277	0.0082	**0.0047**
	3E6	0.0857	0.0615	**0.0591**	0.0147	0.0090	**0.0071**
	6E6	0.0742	**0.0378**	0.0428	0.0120	0.0048	**0.0042**
	9E6	0.0476	**0.0367**	0.0421	0.0053	0.0041	**0.0039**
ROI 4	5E5	0.1542	0.1102	**0.0657**	0.0557	0.0358	**0.0125**
	1E6	0.1199	0.0928	**0.0551**	0.0401	0.0233	**0.0080**
	3E6	0.0932	0.0804	**0.0478**	0.0228	0.0175	**0.0060**
	6E6	0.0758	0.0648	**0.0477**	0.0174	0.0109	**0.0059**
	9E6	0.0716	0.0447	**0.0361**	0.0133	0.0057	**0.0040**
ROI 5	5E5	0.2673	0.2255	**0.1984**	0.2239	0.1677	**0.1469**
	1E6	0.2554	0.2201	**0.1895**	0.2203	0.1626	**0.1414**
	3E6	0.2403	0.2024	**0.1641**	0.2035	0.1356	**0.1156**
	6E6	0.2302	0.1971	**0.1565**	0.1812	0.1317	**0.0909**
	9E6	0.2200	0.1864	**0.1503**	0.1807	0.1239	**0.0899**

doi:10.1371/journal.pone.0166871.t002

Here, the IST method was used to evaluate the effectiveness of the ADM to solve the TV-problem. The results are shown in Fig 8. The *y*-axis represents relative error and the *x*-axis represents the iteration times of the methods. The black curve represents Poisson-TV, the green curve LS-TV, the yellow curve EM, and the red curve the IST method. For all methods, the relative error approaches close to 0 within 20 iterations (since the stopping threshold is 10^{-3} for all experiments). With the help of the ADM, the relative error of the Poisson-TV and LS-TV decreases to approximately 0.1 with only two iterations, while the relative error of IST decreases to approximately 0.22 and the relative error of EM is 0.65. This shows that the curves of both Poisson-TV and LS-TV decrease faster than those of IST and EM. All the results demonstrate that the convergence speed of the ADM is faster than that of the IST method and much faster than that of the EM method.

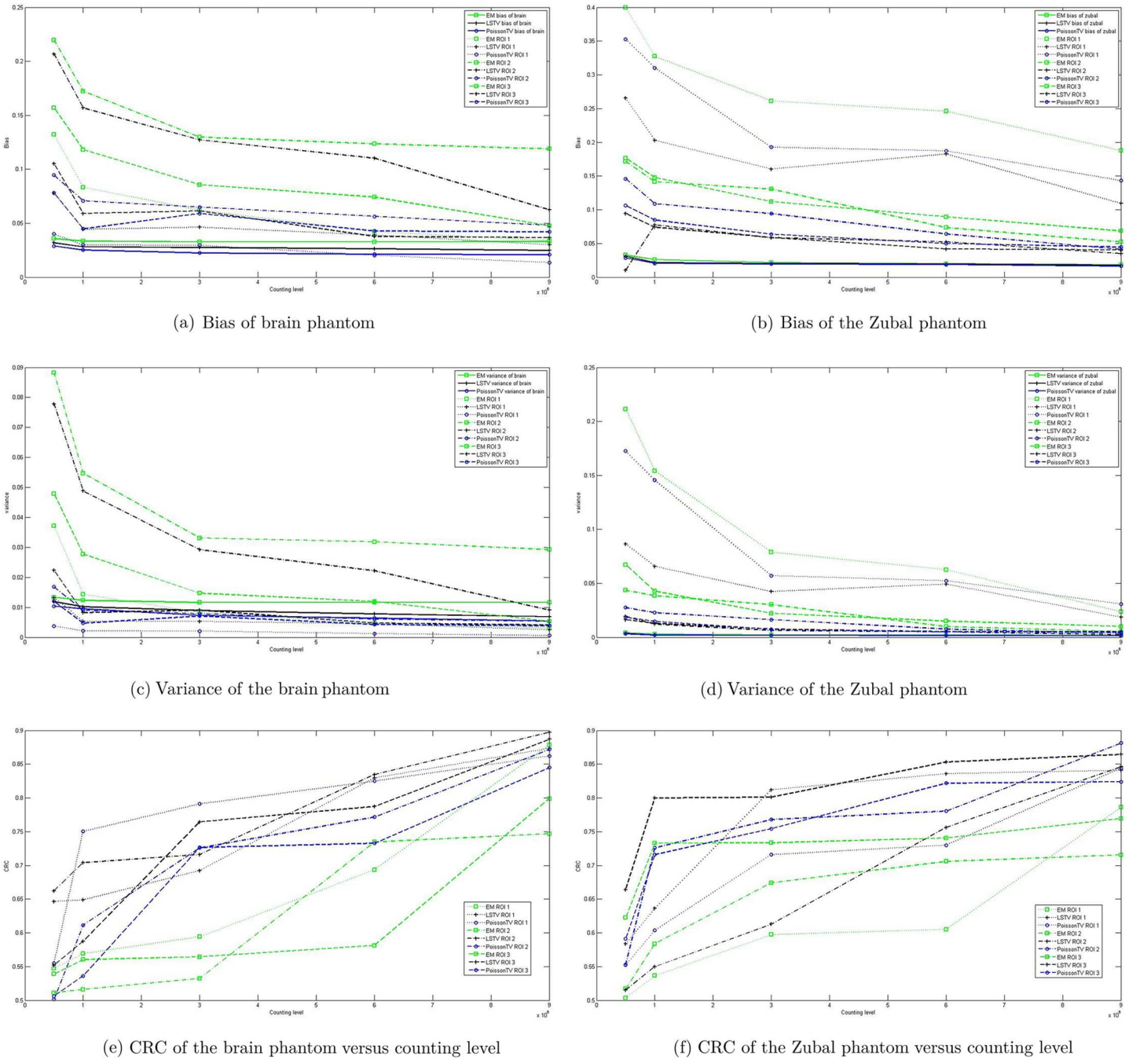

(a) Bias of brain phantom

(b) Bias of the Zubal phantom

(c) Variance of the brain phantom

(d) Variance of the Zubal phantom

(e) CRC of the brain phantom versus counting level

(f) CRC of the Zubal phantom versus counting level

Fig 7. Bias, variance, and CRC profiles for the Zubal phantom and brain phantom with different counts.

doi:10.1371/journal.pone.0166871.g007

Phantom case

In this section, the results of real scanning phantom experiments are presented. The results were obtained under real conditions, in which sinograms were generated by the scan of a Hamamatsu SHR-22000 PET scanner. The phantom used is the Derenzo phantom. There are six sector regions in this phantom. In each sector region, there are several spheres arranged in a triangular array. These spheres have different diameters corresponding to the different spatial

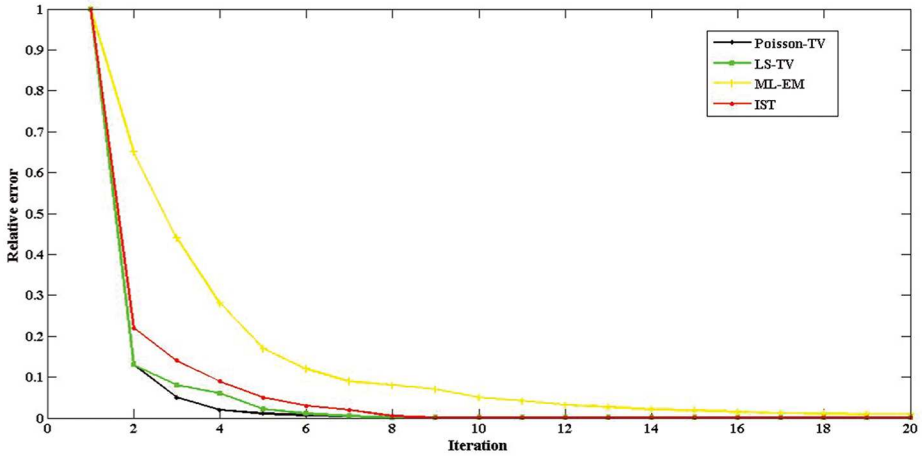

Fig 8. Convergence rate for IST, EM, Poisson-TV, and LS-TV.

doi:10.1371/journal.pone.0166871.g008

resolutions. A $^{18}F - FDG$ solution was injected into the Derenzo phantom. The total counting rate of coincidence events was 10^5. The images reconstructed by the EM, Poisson-TV, and LS-TV methods are shown in Fig 9. To evaluate the detailed information of the reconstruction, the marked areas (marked by a red rectangle) are given in Fig 9(b) and zoomed for comparison. It is clearly indicated that the quality of the recovery, in particular the detailed information yielded by the Poisson-TV and LS-TV methods, is better than that of the EM method.

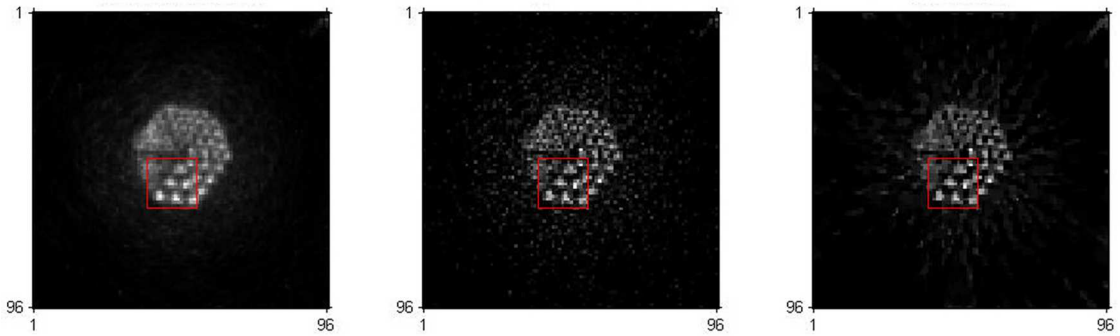

(a) Images (resolution board) reconstructed by EM, Poisson-TV, and LS-TV (from left to right)

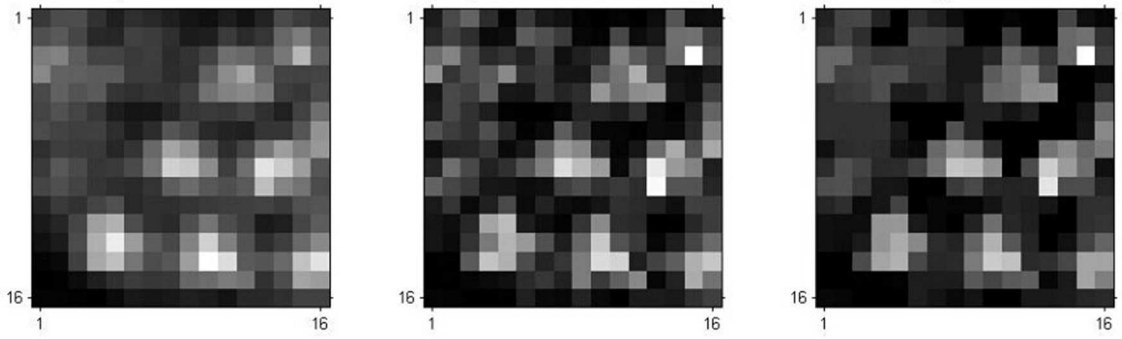

(b) Marked regions of interest in (a)

Fig 9. Reconstruction of the phantom case.

doi:10.1371/journal.pone.0166871.g009

Clinical case

In this section, we validate the proposed method using clinical patient data. The clinical patient data comprised a PET scan acquired from a volunteer at a local hospital. The PET system used was a Hamamatsu SHR-22000 whole body PET scanner. It has 32 crystal rings and can be operated in 2D or 3D mode. The trans-axial resolution of the central FOV is about 3.7 mm. The patient lay on the bed and the main target of the scanning was the thorax. The total scanning time was 40 min. Random, normalization, dead time, scatter, and attenuation correction were applied to the measurement data using the programs provided by the scanner prior to reconstruction. The measurement data were stored in the sinogram model, the size of the reconstructed images was $128 * 128$.

To evaluate the effectiveness of the proposed method, the Poisson-TV, LS-TV, and EM algorithms were used in this experiment. Their results are shown in Fig 10. In Fig 10(a), the difference between these three methods is not sufficiently clear, however, all the algorithms can provide a clear reconstruction. However, when we zoom in on the highlighted region (marked by a red rectangle) in the reconstructed images, it is clear that, as compared to EM, both the Poisson and LS TV algorithm can provide better edge information and better visual quality, in particular for the small highlighted point marked by the red arrow. In the results of the EM algorithm, this point almost disappears in the noise background. In contrast, we can easily locate this point in the results of Poisson-TV and LS-TV. In the comparison of the LS-TV and Poisson-TV, since the results of the LS-TV method suffer from some undesirable

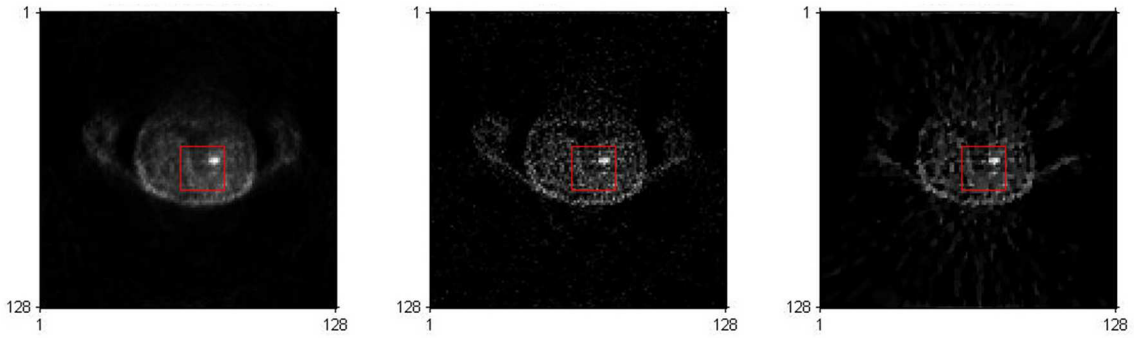

(a) Images (real patient data) reconstructed by EM, Poisson-TV, and LS-TV (from left to right)

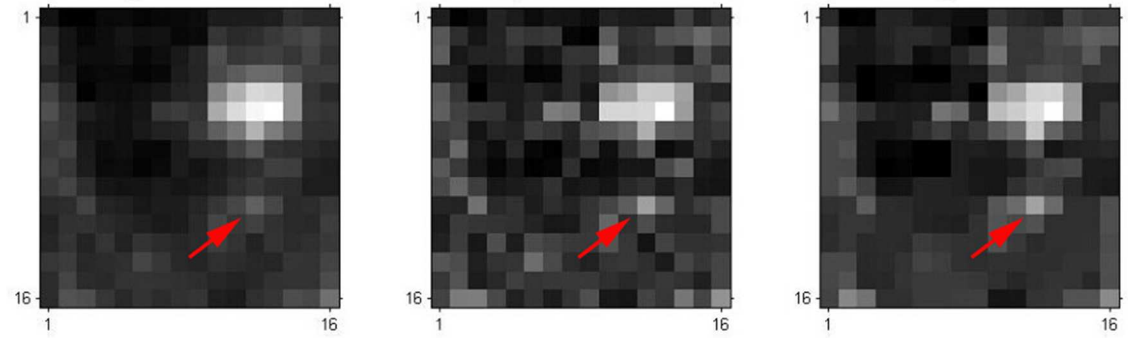

(b) Marked highlight area of interest in (a)

Fig 10. Reconstruction of images for the clinical patient.

doi:10.1371/journal.pone.0166871.g010

artifacts (such as edge over-smoothness and staircase effects), Poisson-TV yields a much better visual quality than LS-TV and recovers more detail of textures in the reconstructed image.

Conclusion

This paper presented a TV-constraint reconstruction algorithm for low dose PET image reconstruction. According to the property of the PET measured data, two types of TV-constraint models, LS-TV and Poisson-TV, were established. To efficiently obtain high quality reconstructed images, the ADM is used. To evaluate the effectiveness of the proposed LS-TV and Poisson-TV methods, PET data measured from a Monte Carlo simulation and real scanning were used. As compared with the traditional EM method, the proposed TV-constraint models are able to reconstruct the images with higher accuracy and much clearer structures. The ADM also provides a faster convergence rate as compared to the IST method for solving the TV problem. Both Poisson-TV and LS-TV can provide a high visual quality and are robust to noise corruptions at a low dose level; Poisson-TV gives a more accurate estimation with lower bias and variances, whereas the CRC of the LS-TV is better. This means that, although both the proposed TV methods can provide a highly accurate and robust reconstruction, Poisson-TV is more suitable for kinetic parameter estimation, which requires a highly accurate estimation with low bias and variance for PET images. In contrast, LS-TV is more suitable for tumor diagnosis, which requires a high contrast for PET images in order to locate the tumor.

Acknowledgments

This work is supported in part by the National Natural Science Foundation of China(No: 61427807, 61271083, 61525106), by National Key Technology Research and Development Program of the Ministry of Science and Technology of China (No: 2016YFC1300302), by the Shenzhen Innovation Funding(SGLH20131010110119871), by Zhejiang Province Science and Technology Projects(No: 2015C33061).

Author Contributions

Conceptualization: XY HL CW.

Data curation: HL XY.

Formal analysis: HH HL.

Methodology: XY CW.

Software: XY CW.

Validation: HL.

Writing – original draft: XY CW.

Writing – review & editing: HL HH.

References

1. Henry T, Chungani H, Abou-Khalil W, Theodore W, Swartz B. Positron emission tomography. Medical Imaging: Principles and Practices. 2012;.
2. Cheng-Liao J, Qi J. PET image reconstruction with anatomical edge guided level set prior. Physics in medicine and biology. 2011; 56(21):6899. doi: 10.1088/0031-9155/56/21/009 PMID: 21983558
3. Shepp LA, Vardi Y. Maximum likelihood reconstruction for emission tomography. Medical Imaging, IEEE Transactions on. 1982; 1(2):113–122. doi: 10.1109/TMI.1982.4307558 PMID: 18238264

4. Gaitanis A, Kontaxakis G, Spyrou G, Panayiotakis G, Tzanakos G. PET image reconstruction: A stopping rule for the MLEM algorithm based on properties of the updating coefficients. Computerized Medical Imaging and Graphics. 2010; 34(2):131–141. doi: 10.1016/j.compmedimag.2009.07.006 PMID: 19744826
5. Hudson HM, Larkin RS. Accelerated image reconstruction using ordered subsets of projection data. Medical Imaging, IEEE Transactions on. 1994; 13(4):601–609. doi: 10.1109/42.363108 PMID: 18218538
6. Hebert T, Leahy R. A generalized EM algorithm for 3-D Bayesian reconstruction from Poisson data using Gibbs priors. Medical Imaging, IEEE Transactions on. 1989; 8(2):194–202. doi: 10.1109/42.24868 PMID: 18230517
7. Green PJ. Bayesian reconstructions from emission tomography data using a modified EM algorithm. Medical Imaging, IEEE Transactions on. 1990; 9(1):84–93. doi: 10.1109/42.52985 PMID: 18222753
8. Cheng JCK, Shoghi K, Laforest R. Quantitative accuracy of MAP reconstruction for dynamic PET imaging in small animals. Medical physics. 2012; 39(2):1029–1041. doi: 10.1118/1.3678489 PMID: 22320813
9. Fessler JA. Penalized weighted least-squares image reconstruction for positron emission tomography. Medical Imaging, IEEE Transactions on. 1994; 13(2):290–300. doi: 10.1109/42.293921 PMID: 18218505
10. Zhou J, Coatrieux JL, Luo L. Noniterative sequential weighted least squares algorithm for positron emission tomography reconstruction. Computerized Medical Imaging and Graphics. 2008; 32(8):710–719. doi: 10.1016/j.compmedimag.2008.08.008 PMID: 18842391
11. Bailey DL, Meikle SR. A convolution-subtraction scatter correction method for 3D PET. Physics in medicine and biology. 1994; 39(3):411. doi: 10.1088/0031-9155/39/3/009 PMID: 15551590
12. Mumcuoglu EU, Leahy R, Cherry SR, Zhou Z. Fast gradient-based methods for Bayesian reconstruction of transmission and emission PET images. Medical Imaging, IEEE Transactions on. 1994; 13 (4):687–701. doi: 10.1109/42.363099 PMID: 18218547
13. Mumcuoglu EÜ, Leahy RM, Cherry SR. Bayesian reconstruction of PET images: methodology and performance analysis. Physics in medicine and Biology. 1996; 41(9):1777. doi: 10.1088/0031-9155/41/9/015 PMID: 8884912
14. Christe SA, Vignesh M, Kandaswamy A. An efficient FPGA implementation of MRI image filtering and tumor characterization using Xilinx system generator. arXiv preprint arXiv:12012542. 2012;.
15. Burger M, Müller J, Papoutsellis E, Schönlieb CB. Total variation regularization in measurement and image space for PET reconstruction. Inverse Problems. 2014; 30(10):105003. doi: 10.1088/0266-5611/30/10/105003
16. Vese LA, Osher SJ. Modeling textures with total variation minimization and oscillating patterns in image processing. Journal of Scientific Computing. 2003; 19(1-3):553–572. doi: 10.1023/A:1025384832106
17. Chan T, Esedoglu S, Park F, Yip A. Recent developments in total variation image restoration. Mathematical Models of Computer Vision. 2005;17. doi: 10.1007/0-387-28831-7_2
18. Chan TF, Esedoglu S, Nikolova M. Algorithms for finding global minimizers of image segmentation and denoising models. SIAM Journal on Applied Mathematics. 2006; 66(5):1632–1648. doi: 10.1137/040615286
19. Chambolle A. An algorithm for total variation minimization and applications. Journal of Mathematical imaging and vision. 2004; 20(1-2):89–97. doi: 10.1023/B:JMIV.0000011325.36760.1e
20. Sawatzky A, Brune C, Müller J, Burger M. Total variation processing of images with Poisson statistics. In: Computer Analysis of Images and Patterns. Springer; 2009. p. 533–540. doi: 10.1007/978-3-642-03767-2_65
21. Goldfarb D, Yin W. Second-order cone programming methods for total variation-based image restoration. SIAM Journal on Scientific Computing. 2005; 27(2):622–645. doi: 10.1137/040608982
22. Alizadeh F, Goldfarb D. Second-order cone programming. Mathematical programming. 2003; 95(1):3–51. doi: 10.1007/s10107-002-0339-5
23. Beck A, Teboulle M. A fast iterative shrinkage-thresholding algorithm for linear inverse problems. SIAM Journal on Imaging Sciences. 2009; 2(1):183–202. doi: 10.1137/080716542
24. Bioucas-Dias JM, Figueiredo MA. A new TwIST: two-step iterative shrinkage/thresholding algorithms for image restoration. Image Processing, IEEE Transactions on. 2007; 16(12):2992–3004. doi: 10.1109/TIP.2007.909319 PMID: 18092598
25. Elad M. Why simple shrinkage is still relevant for redundant representations? IEEE transactions on information theory. 2006; 52(12):5559–5569. doi: 10.1109/TIT.2006.885522

26. Chambolle A, Lions PL. Image recovery via total variation minimization and related problems. Numerische Mathematik. 1997; 76(2):167–188. doi: 10.1007/s002110050258

27. Wu C, Tai XC. Augmented Lagrangian method, dual methods, and split Bregman iteration for ROF, vectorial TV, and high order models. SIAM Journal on Imaging Sciences. 2010; 3(3):300–339. doi: 10.1137/090767558

28. Powell MJ. "A method for non-linear constraints in minimization problems". UKAEA; 1967.

29. Chen C, He B, Yuan X. Matrix completion via an alternating direction method. IMA Journal of Numerical Analysis. 2012; 32(1):227–245. doi: 10.1093/imanum/drq039

30. Yang J, Zhang Y, Yin W. A fast alternating direction method for TVL1-L2 signal reconstruction from partial Fourier data. Selected Topics in Signal Processing, IEEE Journal of. 2010; 4(2):288–297. doi: 10.1109/JSTSP.2010.2042333

31. Wu C, Zhang J, Tai XC. Augmented Lagrangian method for total variation restoration with non-quadratic fidelity. Inverse problems and imaging. 2011; 5(1):237–261. doi: 10.3934/ipi.2011.5.237

32. Wang Y, Yang J, Yin W, Zhang Y. A new alternating minimization algorithm for total variation image reconstruction. SIAM Journal on Imaging Sciences. 2008; 1(3):248–272. doi: 10.1137/080724265

33. Barzilai J, Borwein JM. Two-point step size gradient methods. IMA Journal of Numerical Analysis. 1988; 8(1):141–148. doi: 10.1093/imanum/8.1.141

34. Yuan Yx. Step-sizes for the gradient method. AMS IP STUDIES IN ADVANCED MATHEMATICS. 2008; 42(2):785.

35. Meza JC. Steepest descent. Wiley Interdisciplinary Reviews: Computational Statistics. 2010; 2(6):719–722. doi: 10.1002/wics.117

36. Ye X, Chen Y, Huang F. Computational Acceleration for MR Image Reconstruction in Partially Parallel Imaging. Transactions on Medical Imaging. 2011; 30(5):1055–1063. doi: 10.1109/TMI.2010.2073717 PMID: 20833599

37. Hestenes MR. Multiplier and gradient methods. Journal of optimization theory and applications. 1969; 4(5):303–320. doi: 10.1007/BF00927673

38. Tomioka R, Suzuki T, Sugiyama M. Super-linear convergence of dual augmented Lagrangian algorithm for sparsity regularized estimation. The Journal of Machine Learning Research. 2011; 12:1537–1586.

39. Aguiar P, Xing EP, Figueiredo M, Smith NA, Martins A. An augmented Lagrangian approach to constrained MAP inference. In: Proceedings of the 28th International Conference on Machine Learning (ICML-11); 2011. p. 169–176.

40. Gill PE, Robinson DP. A primal-dual augmented Lagrangian. Computational Optimization and Applications. 2012; 51(1):1–25. doi: 10.1007/s10589-010-9339-1

41. Osher S, Burger M, Goldfarb D, Xu J, Yin W. An iterative regularization method for total variation-based image restoration. Multiscale Modeling & Simulation. 2005; 4(2):460–489. doi: 10.1137/040605412

42. Jan S, Santin G, Strul D, Staelens S, Assie K, Autret D, et al. GATE: a simulation toolkit for PET and SPECT. Physics in medicine and biology. 2004; 49(19):4543. doi: 10.1088/0031-9155/49/19/007 PMID: 15552416

43. Stützer K, Bert C, Enghardt W, Helmbrecht S, Parodi K, Priegnitz M, et al. Experimental verification of a 4D MLEM reconstruction algorithm used for in-beam PET measurements in particle therapy. Physics in medicine and biology. 2013; 58(15):5085. doi: 10.1088/0031-9155/58/15/5085 PMID: 23831685

44. Fessler J, et al. Image reconstruction toolbox. Available at website: http://www.eecs.umich.edu/fessler/code 2012;.